ACS PHYSICAL CHEMISTRY Au
AN OPEN ACCESS JOURNAL OF THE AMERICAN CHEMICAL SOCIETY

pubs.acs.org/physchemau

Article

Excitation-Dependent Anisotropic Raman Response of Atomically Thin Pentagonal $PdSe_2$

Weijun Luo, Akinola D. Oyedele, Nannan Mao, Alexander Puretzky, Kai Xiao, Liangbo Liang,* and Xi Ling*

Cite This: *ACS Phys. Chem Au* 2022, 2, 482–489

Read Online

ACCESS | Metrics & More | Article Recommendations | Supporting Information

ABSTRACT: The group-10 noble-metal dichalcogenides have recently emerged as a promising group of two-dimensional materials due to their unique crystal structures and fascinating physical properties. In this work, the resonance enhancement of the interlayer breathing mode (B1) and intralayer A_g^1 and A_g^3 modes in atomically thin pentagonal $PdSe_2$ were studied using angle-resolved polarized Raman spectroscopy with 13 excitation wavelengths. Under the excitation energies of 2.33, 2.38, and 2.41 eV, the Raman intensities of both the low-frequency breathing mode B1 and high-frequency mode A_g^1 of all the thicknesses are the strongest when the incident polarization is parallel to the *a* axis of $PdSe_2$, serving as a fast identification of the crystal orientation of few-layer $PdSe_2$. We demonstrated that the intensities of B1, A_g^1, and A_g^3 modes are the strongest with the excitation energies between 2.18 and 2.38 eV when the incident polarization is parallel to $PdSe_2$ *a* axis, which arises from the resonance enhancement caused by the absorption. Our investigation reveals the underlying interplay of the anisotropic electron–phonon and electron–photon interactions in the Raman scattering process of atomically thin $PdSe_2$. It paves the way for future applications on $PdSe_2$-based optoelectronics.

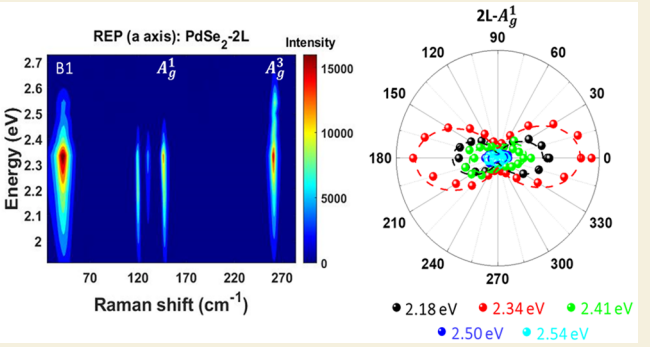

KEYWORDS: *2D anisotropic materials, $PdSe_2$, low-frequency Raman, strong interlayer coupling, electron–phonon interactions*

INTRODUCTION

Pentagonal $PdSe_2$, a representative candidate in the two-dimensional (2D) group-10 noble-metal dichalcogenides, has received broad attention due to its layer-dependent indirect bandgaps from ∼0 eV (bulk) to ∼1.3 eV (monolayer), robust air stability, in-plane anisotropy, and high carrier mobility.[1,2] Specifically, the breakthroughs in $PdSe_2$ synthesis techniques such as the bulk crystal growth[1] and chemical vapor desposition[3,4] of ultrathin $PdSe_2$ have been demonstrated. The rapid progress ignites the studies on the physical properties and device applications of $PdSe_2$, such as thermoelectrics,[5] photodetectors,[6−8] and field-effect transistors (FET).[9−11] Furthermore, studies on the anisotropy of lattice vibrations of both strained[12] and unstrained $PdSe_2$[13] have been reported. However, the in-depth understanding of the anisotropic Raman response of 2D $PdSe_2$ affected by different laser excitation energies remains underexplored.

The electron–photon and electron–phonon interactions in solids play an essential role in the resonant Raman response of anisotropic layered materials. The studies in the Raman response of the anisotropic layered materials such as black phosphorus[14−16] (BP), ReS_2,[17−19] and $ReSe_2$[20] are often complicated by the intricate thickness, stacking order, orientation, and excitation-energy-dependent photon–electron–phonon interactions, which arise from the highly anisotropic electronic band structures and phonon vibrations. Since resonant Raman scattering with a wide range of selective excitation energies could provide much more information on the interband electronic transitions and their interactions with phonons, it has served as a powerful tool in unveiling the anisotropic symmetry-dependent electron–phonon coupling of anisotropic 2D materials[21,22] and heterostructures.[23] For instance, Mao et al.[24] presented systematic studies on the resonance Raman spectroscopy of BP and suggested the explicit anisotropic resonant Raman response with the excitation energy between 2.60 and 2.73 eV. Other work also indicated the unambiguous anisotropic resonant Raman response with excitation energy of 2.81 eV (441.6 nm).[25,26] Nevertheless, the experimental investigations on the resonant Raman response of anisotropic $PdSe_2$ and theoretical understanding of the corresponding electron–photon and electron–

Received: February 2, 2022
Revised: July 15, 2022
Accepted: July 22, 2022
Published: August 4, 2022

https://doi.org/10.1021/acsphyschemau.2c00007
ACS Phys. Chem Au 2022, 2, 482–489

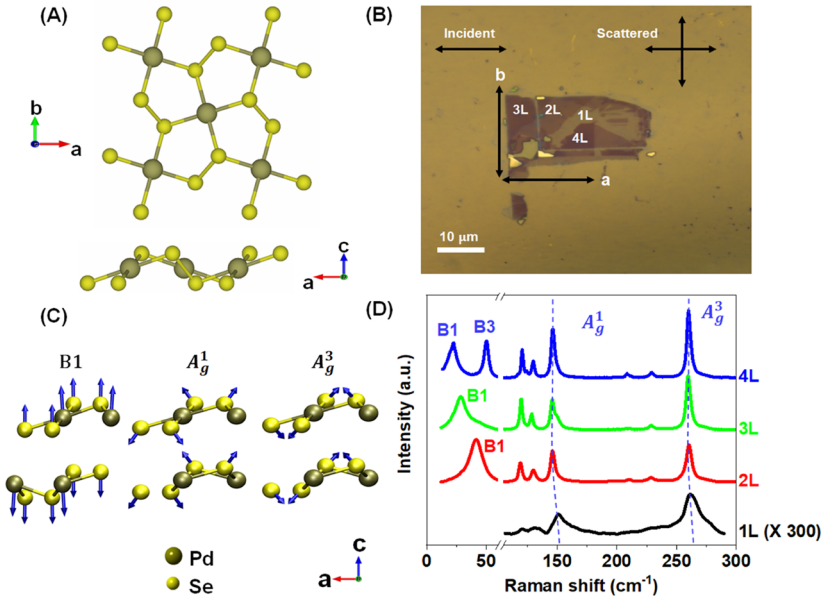

Figure 1. Illustration of the $PdSe_2$ crystal structure and identification of $PdSe_2$ crystal orientations and thicknesses. (A) Crystallographic structure of a 1L 2D pentagonal $PdSe_2$. (B) Optical images of the exfoliated 1−4L $PdSe_2$ studied in this work. (C) Illustration of atomic displacements of B1, A_g^1, and A_g^3 phonon modes. (D) Raman spectra of 1−4L $PdSe_2$ where the laser (532 nm excitation) polarization is along the *a* axis of $PdSe_2$.

phonon interactions are still limited. Recently, Puretzky and co-workers reported the unprecedently strong Raman intensities of low-frequency interlayer vibrations in $PdSe_2$ under 2.33 eV (532 nm excitation).[13] This is quite unusual compared to the weak low-frequency interlayer Raman modes commonly observed in many other layered materials.[27,28] Therefore, a comprehensive study on the $PdSe_2$ low-frequency interlayer phonon response under different resonance conditions is also highly desired.

Herein, we investigated the excitation-energy-dependent and polarized Raman response of both interlayer and intralayer vibrations of atomically thin (1−7 L) pentagonal $PdSe_2$ with 13 excitation laser lines (454−648 nm). We demonstrate that with the excitation energies of 2.41 eV (514 nm), 2.38 eV (520 nm), and 2.33 eV (532 nm), the maximum Raman intensities of B1 and A_g^1 modes appear when the incident laser polarization is along the $PdSe_2$ *a* axis for all the thicknesses. Hence, the crystal orientation of $PdSe_2$ can be identified unambiguously. Via the analysis of resonant excitation profiles, we unveil that Raman intensities of B1, A_g^1 and A_g^3 modes are the strongest under the excitation energy of 2.33 eV (532 nm) when the incident polarization is along the *a* axis of $PdSe_2$. In addition, the A_g^3 mode shows a second strongest Raman intensity under the excitation energy of 2.54 eV (488 nm). Furthermore, the measured absorption results show two broad absorption peaks at 1.9−2.3 and 2.6−3.0 eV, respectively, where the Raman polarizability is promoted and enhances Raman intensities. Therefore, the maximum Raman intensities of B1, A_g^1, and A_g^3 modes appearing at different energy ranges and specific crystal orientations could be attributed to the anisotropic electron−phonon coupling and the symmetry-dependent excited states involved in the resonance Raman scattering. Our work lays the foundation for further studies and applications on $PdSe_2$-based optoelectronic devices.

RESULTS AND DISCUSSION

The $PdSe_2$ crystal structure with a unique pentagonal configuration is illustrated in Figure 1(A). A single layer of $PdSe_2$ has a periodic corrugated structure; each Pd atom is connected to four Se atoms, while each Se atom is bonded with two Pd atoms and another Se atom. Pentagonal $PdSe_2$ exhibits layer-dependent crystal symmetries:[13] the bulk $PdSe_2$ crystal (> 20 L) belongs to *Pbca* (#61) space group symmetry and D_{2h} point group symmetry; for the odd-layer $PdSe_2$, its crystal symmetry reduces to the point group C_{2h} ($2/m$) with the space group belonging to $P2_1/c$ (#14). In contrast, even-layer $PdSe_2$ belongs to space group $Pca2_1$ (#29) and point group C_{2v} ($mm2$).

Figure 1(B) shows a typical exfoliated $PdSe_2$ sample on a 285 nm SiO_2/Si substrate, with the black arrow representing the horizontal polarization of the incident laser as explained in the Methods section. Note that different numbers of layers of $PdSe_2$ in the same flake have the same crystallographic orientation. The exfoliated $PdSe_2$ flakes tend to cleave along their two principal crystal axes ([100] and [010]), which often results in the rectangular shapes, where the long and short edges are along the $PdSe_2$ *a* axis ([100] direction) and the *b* axis ([010] direction), respectively.[3,12] Also, the two principal $PdSe_2$ crystal axes were further characterized and shown in Figure S1(A−D), where the maximum Raman intensities of B1 (2 − 4 L) and A_g^1 modes (1 − 4 L) appear when the laser polarization is parallel to the $PdSe_2$ *a* axis (long edge) under 532 nm excitation, which agrees with previous studies.[12,13]

Figure 1(C) illustrates the atomic displacements of the low-frequency breathing mode B1 and two high-frequency modes A_g^1 and A_g^3: B1 represents all the atoms vibrating out of the plane, A_g^1 is affected by the in-plane vibration of covalently bonded Pd and Se atoms, and A_g^3 is affected by the in-plane vibration of two neighboring covalently bonded Se atoms. Figure S2 includes more details of the vibration patterns of A_g^1 and A_g^3 modes.

Figure 1(D) shows the corresponding Raman spectra of different locations, and their thicknesses are determined explicitly by their low-frequency (LF) interlayer Raman fingerprints (<100 cm^{-1}). Following the previous works,[12,13] the LF modes' notations are assigned, and their frequencies are

https://doi.org/10.1021/acsphyschemau.2c00007
ACS Phys. Chem Au 2022, 2, 482−489

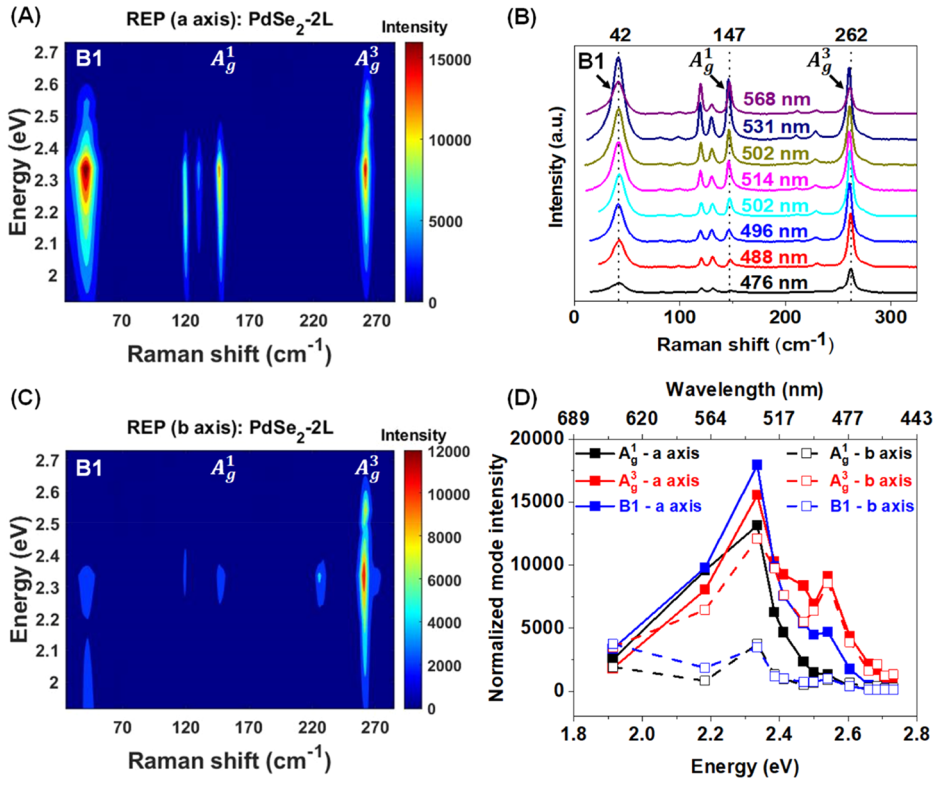

Figure 2. (A,C) Resonant excitation profiles (REPs) after normalization (by using the Raman peak intensity of a single-crystal quartz substrate at ~465 cm^{-1}) of a 2L $PdSe_2$ sample with the laser polarization along the $PdSe_2$ *a* and *b* axes, respectively. (B) Raman spectra of bilayer $PdSe_2$ are excited by eight laser lines from 476 to 568 nm, and the laser polarization is parallel to the $PdSe_2$ *a* axis. (D) Summary of normalized intensities of B1, A_g^1, and A_g^3 modes under different excitation energies after the interference effects are removed, with the laser polarization along the $PdSe_2$ *a* and *b* axes, respectively.

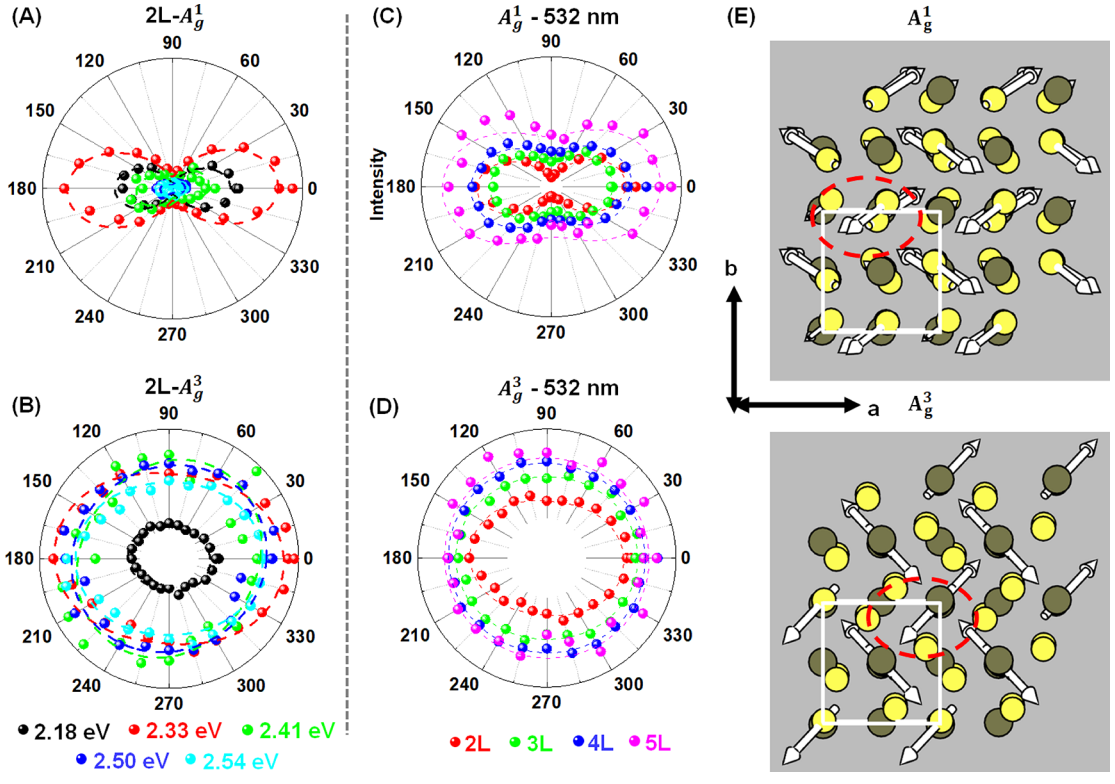

Figure 3. (A,B) Raman intensity polar plots of A_g^1 and A_g^3 modes of 2L $PdSe_2$ excited by different laser photon energies. (C,D) Raman intensity polar plots of A_g^1 and A_g^3 modes of 2−5L $PdSe_2$ with 532 nm laser excitation. (E) Computed vibration patterns of $PdSe_2$ A_g^1 and A_g^3 phonons.

https://doi.org/10.1021/acsphyschemau.2c00007
ACS Phys. Chem Au 2022, 2, 482−489

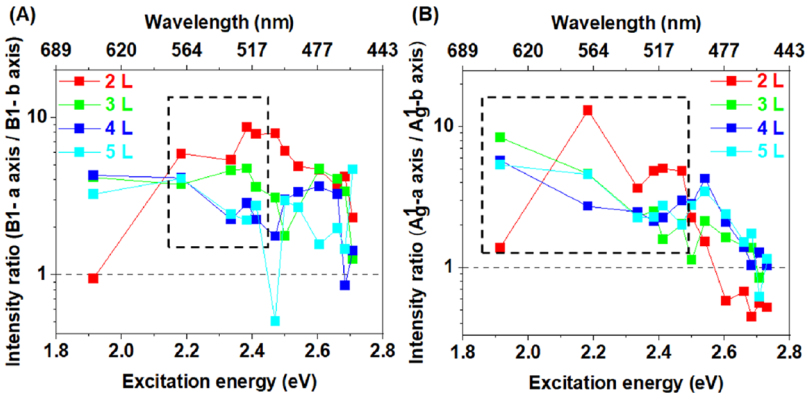

Figure 4. (A) Ratios of the normalized intrinsic Raman intensity of $\frac{I_{B1//a}}{I_{B1//b}}$ in 2−5L $PdSe_2$. (B) Ratios of the normalized intrinsic Raman intensity of $\frac{I_{A_g^1//a}}{I_{A_g^1//b}}$ in 2−5L $PdSe_2$.

summarized in Figure S3(A). Moreover, for monolayer $PdSe_2$, A_g^1 and A_g^3 Raman frequencies are at ∼150 and ∼263 cm^{-1}, respectively; for 2L $PdSe_2$ and above thicknesses, their Raman frequencies are at ∼145 and ∼258 cm^{-1}, respectively, which agrees with previous work.[1] In addition, the Raman spectra of monolayer and three bulk $PdSe_2$ flakes (F1−F3) in the same crystal are shown in Figure S3(B) for comparison.

After the thickness and crystal axes were determined, the excitation-energy-dependent Raman modes of bilayer $PdSe_2$ were analyzed. In specific, we focused on the B1, A_g^1 (∼150 cm^{-1}), and A_g^3 (∼263 cm^{-1}) modes due to their strong intensities among all $PdSe_2$ Raman modes and thicknesses.

Figure 2(A) shows the resonance excitation profiles (REPs) obtained at the *a* axis of bilayer $PdSe_2$: B1, A_g^1, and A_g^3 Raman intensities all maximize at 2.33 eV (532 nm) excitation; A_g^3 modes also show the second strongest intensities at 2.54 eV (488 nm), supported by Figure 2(D), where the mode intensities at different directions under all excitation energies were summarized. Figure 2(B) shows the representative Raman spectra of bilayer $PdSe_2$ excited by eight laser lines from 2.61 eV (476 nm) to 2.18 eV (568 nm). The low-frequency B1 mode shows the strongest intensity at 2.33 eV (532 nm) excitation; it then reduces notably with increasing excitation energies. Figure 2(C) shows the complete REPs obtained at the *b* axis of bilayer $PdSe_2$: the A_g^3 mode shows its strongest Raman intensity with 2.33 eV (532 nm) excitation. However, B1 and A_g^1 Raman intensities decrease with increasing excitation energies from 2.54 eV (488 nm) and become utterly unnoticeable from 2.66 eV (466 nm) and 2.68 eV (462 nm), respectively; the A_g^3 mode remains visible at all excitation energies despite decreasing with increasing excitation energies from 2.54 eV (488 nm). Figure 2(D) summarizes the intensities of B1, A_g^1, and A_g^3 modes under different excitation energies of bilayer $PdSe_2$: between the excitation energies of 2.18 eV (568 nm) and 2.41 eV (514 nm), B1 and A_g^1 modes show significantly stronger intensities when the incident polarization is at the *a* axis of bilayer $PdSe_2$, while those of A_g^3 are almost similar at both the *a* and *b* axes of bilayer $PdSe_2$ across all the excitation energies. The mode intensities of B1, A_g^1, and A_g^3 of other few-layer samples (1 L, 3 − 7 L) and the A_g^1 and A_g^3 of three thick flakes (30, 35, and 80 nm) are summarized in Figures S4 and S5.

The polar plots describing the angle-dependent mode intensities and mode intensity ratios are investigated to gain more insights from the anisotropic Raman intensities at different orientations. Note that similar approaches have been utilized to study the electron−phonon interactions in black phosphorus,[14−16,24] ReS_2,[20] and $ReSe_2$,[29] which are often intricated due to different thickness and excitation energies. The interference enhancement effects that influence the Raman intensities were computed and excluded to get the intrinsic Raman intensities (see more details in Figures S6 and S7). Figure 3(A,B) shows the angle-resolved polarized Raman results of A_g^1 and A_g^3 phonons of bilayer $PdSe_2$ excited by laser photon energies from 2.18 to 2.54 eV: the A_g^1 modes always show the strongest intensities when the incident polarization is along the $PdSe_2$ *a* axis, while the A_g^3 mode intensities have negligible variations along different crystal orientations. Moreover, the mode intensities of A_g^1 and A_g^3 of different numbers of layers (2 − 5 L) with an excitation energy of 2.33 eV (532 nm) are shown in Figure 3(C,D), suggesting the A_g^1 modes show their strongest intensities when the incident polarization is along the $PdSe_2$ *a* axis for 2−5L $PdSe_2$, and the A_g^3 mode intensities are insensitive to the incident polarization for 2−5L $PdSe_2$.

More data for other thicknesses and excitation energies can be referred to Figures S8 and S9. In Figures S8(A−E), we compare Raman intensity polar plots of the low-frequency breathing modes B1, B3, and B5 with A_g symmetry and high-frequency A_g^1 phonons for different thickness samples excited by the same laser photon energy of 2.33 eV (532 nm): all the results exhibit explicit dumbbell patterns; specifically, B1 and A_g^1 mode intensities always maximize and minimize at the $PdSe_2$ *a* axis (0°) and the *b* axis (90°) respectively. Moreover, Figure S9(A−F) shows Raman intensity polar plots of the low-frequency B1 and high-frequency A_g^1 phonons of the same thicknesses (2 L, 4L, and 6 L) excited by the different laser photon energies from 1.91 eV (648 nm) to 2.61 eV (476 nm): mode intensities of B1 and A_g^1 always maximize and minimize at the $PdSe_2$ *a* axis (0°) and the *b* axis (90°), respectively. Furthermore, we inferred that only three excitation energies, 2.33 eV (532 nm), 2.38 eV (520 nm), and 2.41 eV (514 nm), would result in B1 and A_g^1 mode intensities always maximizing and minimizing at the $PdSe_2$ *a* axis (0°) and the *b* axis (90°) through the analysis of the mode intensity ratios $\frac{I_{B1//a}}{I_{B1//b}}$ and $\frac{I_{A_g^1//a}}{I_{A_g^1//b}}$ shown in Figures 4(A−B) and S10(A−D). In short, the angle-dependent polarized Raman spectroscopy with the excitation energies of 2.33 eV (532 nm), 2.38 eV (520 nm), and 2.41 eV

https://doi.org/10.1021/acsphyschemau.2c00007
ACS Phys. Chem Au 2022, 2, 482−489

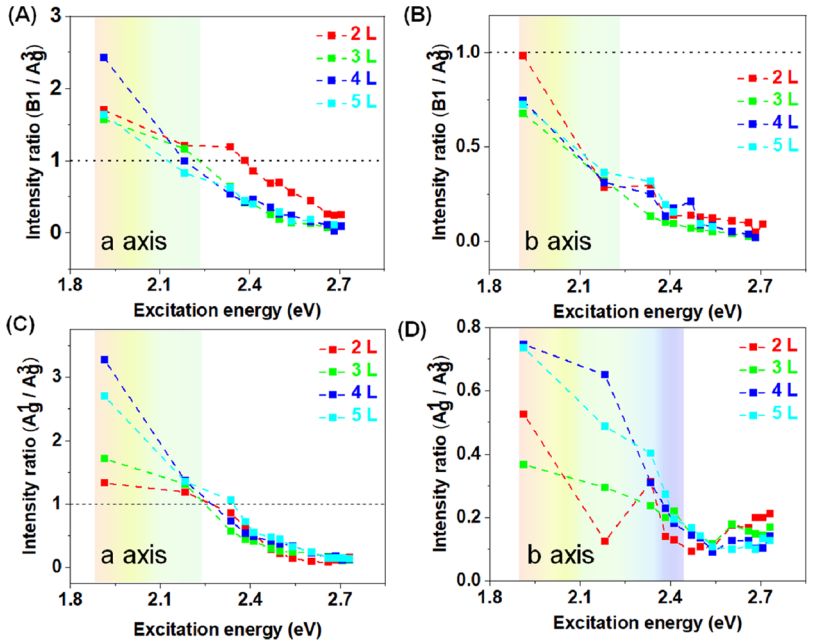

Figure 5. (A,B) Ratios of the normalized intrinsic Raman intensity of $\frac{I_{B1}}{I_{A_g^3}}$ with the laser polarization parallel to the $PdSe_2$ *a* axis (A) and the *b* axis (B). (C,D) Ratios of the normalized intrinsic Raman intensity of $\frac{I_{A_g^1}}{I_{A_g^3}}$ with the laser polarization along the $PdSe_2$ *a* axis (C) and the *b* axis (D).

(514 nm) could serve as a fast and efficient approach for identifying the crystal orientation of few-layer $PdSe_2$.

To probe the origins of different angle-dependent behaviors of B1, A_g^1, and A_g^3 mode intensities, we performed analysis on their computed vibrational patterns. Note that the phonon vibration direction affects the electron−phonon interactions in anisotropic 2D materials significantly.[24] For instance, Mao et al. differentiated the strengths of electron−phonon interactions of black phosphorus's A_g phonons via the analysis of phonon vibrational patterns and relative mode intensity ratios.[24] Figure 3(E) illustrates the simulation results by the density functional theory (DFT) approach: the top-view atomic displacements of A_g^1 and A_g^3 modes in $PdSe_2$, respectively. The vibration of the A_g^1 mode is preferentially along the $PdSe_2$ *a* axis with the Se atoms vibrating roughly 30° along the $PdSe_2$ *a* axis. In contrast, the A_g^3 mode is influenced by the Se atoms vibrating roughly 45° to both the $PdSe_2$ *a* and *b* axes, implying that its vibration is less orientation-selective. Hence, the electronic transition dipole that is preferentially coupled to the linear laser polarization along the *a* axis rather than along the *b* axis gives rise to the stronger Raman intensity of the coupled A_g^1 phonon along the *a* axis; for the A_g^3 mode, changing the laser polarization from the direction of the *a* to the *b* axis does not affect its electron−phonon coupling. Although all the atoms vibrate almost vertically out-of-plane for the B1 mode, it does not prefer a certain in-plane crystal orientation. We also noticed that the low-frequency B1 mode shares similar electron−phonon coupling behavior with the high-frequency A_g^1 mode (see the polar diagrams of the B1 mode in Figures S8 and S9). Such a similarity arises from the stronger-than-vdW interlayer coupling (due to the covalent contribution) and the unique atomic structure with two different types of atoms in each layer of $PdSe_2$.[1] In addition, the displacement of intralayer covalent bonds would contribute to the breathing vibrations and result in the electron−phonon coupling behavior of B1 that might resemble some high-frequency modes.[13]

To gain more insights into the anisotropic electron−phonon interactions in B1, A_g^1, and A_g^3 phonons, we compared their Raman intensity ratios. Figure 4(A,B) shows the Raman intensity ratios $\frac{I_{B1//a}}{I_{B1//b}}$ and $\frac{I_{A_g^1//a}}{I_{A_g^1//b}}$ of 2−5L $PdSe_2$ along the *a* and *b* axes, respectively: with excitation energies from 2.18 eV (568 nm) to 2.54 eV (488 nm), both $\frac{I_{B1//a}}{I_{B1//b}}$ and $\frac{I_{A_g^1//a}}{I_{A_g^1//b}}$ are larger than 1. More data of the other thicknesses are shown in Figure S10(A,B): with excitation energies from 2.33 eV (532 nm) to 2.41 eV (514 nm), both $\frac{I_{B1//a}}{I_{B1//b}}$ and $\frac{I_{A_g^1//a}}{I_{A_g^1//b}}$ are larger than 1; Figure S10(C,D) suggests that the mode intensity ratio of $\frac{I_{A_g^3//a}}{I_{A_g^3//b}}$ for all the studied thicknesses and excitation energies is generally close to 1, which supports that A_g^3 couples similarly with the incident light polarization along both the $PdSe_2$ *a* and *b* axes, as discussed above, based on its vibration pattern.

Furthermore, the intrinsic Raman intensities of B1, A_g^1, and A_g^3 phonons were extracted and are shown in Figure S11(A−F): when the incident polarization is along the *a* axis of $PdSe_2$, the B1 and A_g^1 modes show their strongest intensities between the excitation energies of 1.91 eV (648 nm) and 2.33 eV (532 nm); A_g^3 modes show the strongest intensities between 2.61 eV (476 nm) and 2.68 eV (462 nm) excitation. When the incident polarization is along the *b* axis of $PdSe_2$, the maximum B1 and A_g^1 mode intensities generally appear under the excitation energies of 2.33 eV (532 nm) and 2.68 eV (462 nm); A_g^3 modes show their strongest intensities with excitation energies between ∼2.6 eV (476 nm) and 2.68 eV (462 nm), similar to the case when the incident polarization is along the *a* axis of $PdSe_2$. On the other hand, the absorption measurements of few-layer $PdSe_2$ (as shown in Figure S12) indicate two broad absorption peaks centered at ∼2.3 eV (full width at half maximum (fwhm) of ∼0.3 eV) and ∼2.9 eV (fwhm of ∼0.3

https://doi.org/10.1021/acsphyschemau.2c00007
ACS Phys. Chem Au 2022, 2, 482−489

eV), which match with the strong resonance conditions of B1, A_g^1, and A_g^3 phonons, respectively. Meanwhile, a recent work[30] demonstrated the orientation-dependent absorption of few-layer $PdSe_2$, where the lower energy absorption peak exhibits a blue shift when the incident polarization switches from the $PdSe_2$ *a* axis to the *b* axis. Such a transition matches the trend mentioned above. Therefore, the anisotropic absorption dominates the discrepancies of resonance conditions of B1, A_g^1, and A_g^3 modes along with different incident polarizations.

Moreover, the relative strengths of the electron−phonon interaction among the B1, A_g^1, and A_g^3 modes were compared by calculating the intensity ratios of $\frac{I_{B1}}{I_{A_g^3}}$ and $\frac{I_{A_g^1}}{I_{A_g^3}}$ as a function of the excitation energy. As shown in Figures 5(A,C), for 2−5L $PdSe_2$, the intensity ratios of $\frac{I_{B1}}{I_{A_g^3}}$ and $\frac{I_{A_g^1}}{I_{A_g^3}}$ are both larger than 1 under the excitation energies of 1.91 eV (648 nm) and 2.18 eV (568 nm) when the laser polarization is along the $PdSe_2$ *a* axis, indicating the stronger electron−phonon coupling of B1 and A_g^1 along the *a* axis than that of A_g^3 along the *a* axis. However, with larger excitation energies, the ratios start decreasing to less than 1, suggesting that the electron−phonon coupling of A_g^3 along the $PdSe_2$ *a* axis surpasses those of B1 and A_g^1 modes; on the other hand, as shown in Figure 5(B,D), for 2−5L $PdSe_2$, the ratios of $\frac{I_{B1}}{I_{A_g^3}}$ and $\frac{I_{A_g^1}}{I_{A_g^3}}$ are always less than 1 when the laser polarization is along the $PdSe_2$ *b* axis, suggesting that the electron−phonon coupling of A_g^3 along the *b* axis is always larger than those of B1 and A_g^1 for all the excitation energies. Such a trend also agrees roughly with the previous discussion of resonant energy windows for B1, A_g^1, and A_g^3 modes: 1.91 eV (648 nm)−2.33 eV (532 nm) for B1 and A_g^1 phonons and 2.61 eV (476 nm)−2.68 eV (462 nm) excitation for the A_g^3 mode. More data for other thicknesses are shown in Figure S13(A−D), which show consistent results with those for 2 − 5 L. Nonetheless, no distinct trend was observed for the ratios of $\frac{I_{B1}}{I_{A_g^1}}$: as shown in Figure S14(A−D), the excitation-energy-dependent ratios of $\frac{I_{B1}}{I_{A_g^1}}$ fluctuate around ∼1 for most thicknesses with incident polarization along both the $PdSe_2$ *a* and *b* axes. To summarize, the distinct similar trend of $\frac{I_{B1}}{I_{A_g^3}}$ and $\frac{I_{A_g^1}}{I_{A_g^3}}$ suggests that the electron−phonon interactions of the low-frequency B1 mode resemble that of the high-frequency A_g^1 mode, which is further supported by their mode intensity ratios $\frac{I_{B1}}{I_{A_g^1}}$.

CONCLUSION

We presented comprehensive investigations on the resonant Raman response of atomically thin $PdSe_2$ (1 − 7 L) with 13 excitation wavelengths covering the visible range. Under the excitation energies of 2.33, 2.38, and 2.41 eV, the intrinsic interlayer B1 and intralayer A_g^1 mode intensities are the strongest when the incident polarization is along $PdSe_2$ *a* axis, serving as a convenient method for fast and unambiguous identification of the crystal orientation of few-layer $PdSe_2$. In contrast, the intralayer A_g^3 mode intensities are insensitive to the incident polarization. Our DFT simulation results reveal that the vibration of A_g^3 mode is dominated by the Se atoms vibrating roughly 45° to both the $PdSe_2$ *a* and *b* axes, suggesting a weaker mode anisotropy and leading to the similar Raman intensities measured at different orientations. Also, among all the excitation wavelengths, the intrinsic B1 and A_g^1 mode intensities generally maximize between 520 nm (2.38 eV) and 648 nm (1.91 eV) when the incident polarization is parallel to the *a* axis of $PdSe_2$; the intrinsic A_g^3 mode intensities generally maximize under 466 nm (2.66 eV) and 454 nm (2.73 eV). Meanwhile, the absorption measurements reveal two broad peaks at 1.9 − 2.3 and 2.6 − 3.0 eV, respectively. Hence, we attributed that the maximum B1, A_g^1, and A_g^3 Raman intensities appear at different excitation wavelength ranges and specific crystal orientations to the anisotropic electron−phonon coupling and the symmetry-dependent excited states involved in the resonance Raman scattering. Moreover, we illustrated that the trend and strength of electron−phonon interactions in the low-frequency B1 mode are similar to the high-frequency mode A_g^1 for all the thicknesses and photon energies studied here. This comprehensive investigation of the anisotropic Raman response of $PdSe_2$ would shed light on future Raman studies of 2D materials and the development of $PdSe_2$-based optoelectronics.

METHODS

$PdSe_2$ thin flakes were first mechanically exfoliated onto a 300 nm SiO_2/Si wafer using Nitto SPV 224R blue tape from a bulk $PdSe_2$ single crystal that was synthesized using a self-flux method.[1] The thicknesses of the bulk flakes were characterized by a Veeco Dimension 3000 atomic force microscope (AFM), while those thinner ones (1 − 7 L) were characterized by their characteristic ultralow frequency Raman modes. All Raman measurements were performed using a Horiba T64000 triple-grating micro-Raman system with a backscattering configuration using 13 different excitation energies from 1.91 eV (648 nm) to 2.73 eV (454 nm) (Ar/Kr, Coherent Innova 70C). A 100× Olympus (NA = 0.95) objective lens and an 1800 g/mm groove grating were selected to collect and disperse Raman signals.

The angle-resolved Raman measurements were performed to find and distinguish the two main axes (i.e., *a* and *b* axes) of 10 $PdSe_2$ flakes (1−7 L, ∼30, ∼35, and 80 nm). All Raman spectra were collected under the parallel configuration, where the scattered light polarization is parallel to that of the incident light by using an analyzer. $PdSe_2$ samples were rotated every 15° to change the relative angle between their crystal orientations and the laser polarization. The laser power was controlled at 0.5 mW (±1%) for each excitation energy. All the collected Raman spectra were calibrated using the Raman peak intensity of a single-crystal quartz substrate at ∼465 cm^{-1} to eliminate the discrepancy of the instrumental response under different excitation energies.

Plane-wave DFT calculations were carried out using the Vienna Ab initio Simulation Package[31,32] (VASP) with projector augmented wave (PAW) pseudopotentials[31,33,34] for electron−ion interactions, and the generalized gradient approximation (GGA) functional of Perdew, Burke, and Ernzerhof[34] (PBE) for exchange-correlation interactions. Based on the bulk $PdSe_2$ structure (Materials-project database[35]), the original strain-free 1−3L $PdSe_2$ was modeled by creating a periodic slab with a vacuum separation of more than 22 Å to avoid the interactions with periodic images in the out-of-plane direction (*Z* direction). A cutoff energy of 350 eV and 6 × 6 × 1 k-point samplings were used for the optimization of the unit cell (both atomic positions and in-plane lattice constants) until the maximum force allowed on each atom was less than 0.001 eV/Å. The total volume of the structures was fixed during geometry optimization to avoid the structural collapse of the 2D slabs with vacuum separations.

https://doi.org/10.1021/acsphyschemau.2c00007
ACS Phys. Chem Au 2022, 2, 482−489

■ ASSOCIATED CONTENT

Supporting Information

The Supporting Information is available free of charge at https://pubs.acs.org/doi/10.1021/acsphyschemau.2c00007.

Detailed descriptions of the characterizations (angle-polarized Raman spectroscopy, absorption spectroscopy, and AFM), analytical results (normalized mode Raman intensities and mode intensity ratios), and detailed DFT simulation results of Raman mode assignments, visualization of Raman mode vibration patterns, dielectric functions, refractive index, and calculations of interference enhancement (PDF)

■ AUTHOR INFORMATION

Corresponding Authors

Xi Ling − *Department of Chemistry, Division of Materials Science and Engineering, and The Photonics Center, Boston University, Boston, Massachusetts 02215, United States;* orcid.org/0000-0003-3462-9088; Email: xiling@bu.edu

Liangbo Liang − *Center for Nanophase Materials Sciences, Oak Ridge National Laboratory, Oak Ridge, Tennessee 37831, United States;* orcid.org/0000-0003-1199-0049; Email: liangl1@ornl.gov

Authors

Weijun Luo − *Department of Chemistry, Boston University, Boston, Massachusetts 02215, United States*

Akinola D. Oyedele − *Center for Nanophase Materials Sciences, Oak Ridge National Laboratory, Oak Ridge, Tennessee 37831, United States; Bredesen Center for Interdisciplinary Research and Graduate Education, University of Tennessee, Knoxville, Tennessee 37996, United States*

Nannan Mao − *Department of Chemistry, Boston University, Boston, Massachusetts 02215, United States; Department of Electrical Engineering and Computer Science, Massachusetts Institute of Technology, Cambridge, Massachusetts 02139, United States;* orcid.org/0000-0003-3522-5341

Alexander Puretzky − *Center for Nanophase Materials Sciences, Oak Ridge National Laboratory, Oak Ridge, Tennessee 37831, United States;* orcid.org/0000-0002-9996-4429

Kai Xiao − *Center for Nanophase Materials Sciences, Oak Ridge National Laboratory, Oak Ridge, Tennessee 37831, United States;* orcid.org/0000-0002-0402-8276

Complete contact information is available at: https://pubs.acs.org/10.1021/acsphyschemau.2c00007

Notes

The authors declare no competing financial interest.

■ ACKNOWLEDGMENTS

This material is based upon work supported by the National Science Foundation (NSF) under Grant No. (1945364). W.L. and X.L. acknowledge the financial support from Boston University. X.L. acknowledges the membership of the Boston University Photonics Center. We acknowledge the computational resources of the Compute and Data Environment for Science (CADES) at the Oak Ridge National Laboratory, which is supported by the Office of Science of the U.S. Department of Energy under Contract No. DE-AC05-00OR22725, and we also used resources of the National Energy Research Scientific Computing Center, a DOE Office of Science User Facility supported by the Office of Science of the U.S. DOE under Contract No. DE-AC02-05CH11231. Absorption measurements and DFT calculations were supported by the Center for Nanophase Materials Sciences (CNMS), which is a US Department of Energy, Office of Science User Facility at Oak Ridge National Laboratory. W.L. also acknowledges the high-performance computing resources of the Boston University Shared Computing Cluster (SCC).

■ REFERENCES

(1) Oyedele, A. D.; Yang, S.; Liang, L.; Puretzky, A. A.; Wang, K.; Zhang, J.; Yu, P.; Pudasaini, P. R.; Ghosh, A. W.; Liu, Z.; et al. PdSe2: Pentagonal Two-Dimensional Layers with High Air Stability for Electronics. *J. Am. Chem. Soc.* **2017**, *139* (40), 14090−14097.

(2) Oyedele, A. D.; Yang, S.; Feng, T.; Haglund, A. V.; Gu, Y.; Puretzky, A. A.; Briggs, D.; Rouleau, C. M.; Chisholm, M. F.; Unocic, R. R.; Mandrus, D.; Meyer, H. M.; Pantelides, S. T.; Geohegan, D. B.; Xiao, K. Defect-Mediated Phase Transformation in Anisotropic Two-Dimensional PdSe2 Crystals for Seamless Electrical Contacts. *J. Am. Chem. Soc.* **2019**, *141* (22), 8928−8936.

(3) Gu, Y.; Cai, H.; Dong, J.; Yu, Y.; Hoffman, A. N.; Liu, C.; Oyedele, A. D.; Lin, Y.-C.; Ge, Z.; Puretzky, A. A.; et al. Two-Dimensional Palladium Diselenide with Strong In-Plane Optical Anisotropy and High Mobility Grown by Chemical Vapor Deposition. *Adv. Mater.* **2020**, *32*, 1906238.

(4) Lu, L.-S.; Chen, G.-H.; Cheng, H.-Y.; Chuu, C.-P.; Lu, K.-C.; Chen, C.-H.; Lu, M.-Y.; Chuang, T.-H.; Wei, D.-H.; Chueh, W.-C.; et al. Layer-Dependent and In-Plane Anisotropic Properties of Low-Temperature Synthesized Few-Layer PdSe2 Single Crystals. *ACS Nano* **2020**, *14* (4), 4963−4972.

(5) Zhao, Y.; Yu, P.; Zhang, G.; Sun, M.; Chi, D.; Hippalgaonkar, K.; Thong, J. T.; Wu, J. Low-Symmetry PdSe2 for High Performance Thermoelectric Applications. *Adv. Funct. Mater.* **2020**, *30*, 2004896.

(6) Zhang, G.; Amani, M.; Chaturvedi, A.; Tan, C.; Bullock, J.; Song, X.; Kim, H.; Lien, D.-H.; Scott, M. C.; Zhang, H.; et al. Optical and Electrical Properties of Two-Dimensional Palladium Diselenide. *Appl. Phys. Lett.* **2019**, *114* (25), 253102.

(7) Pi, L.; Hu, C.; Shen, W.; Li, L.; Luo, P.; Hu, X.; Chen, P.; Li, D.; Li, Z.; Zhou, X.; et al. Highly In-Plane Anisotropic 2D PdSe2 for Polarized Photodetection with Orientation Selectivity. *Adv. Funct. Mater.* **2021**, *31*, 2006774.

(8) Liang, Q.; Wang, Q.; Zhang, Q.; Wei, J.; Lim, S. X.; Zhu, R.; Hu, J.; Wei, W.; Lee, C.; Sow, C.; et al. High-Performance, Room Temperature, Ultra-Broadband Photodetectors Based on Air-Stable PdSe2. *Adv. Mater.* **2019**, *31* (24), 1807609.

(9) Giubileo, F.; Grillo, A.; Iemmo, L.; Luongo, G.; Urban, F.; Passacantando, M.; Di Bartolomeo, A. Environmental Effects on Transport Properties of PdSe2 Field Effect Transistors. *Mater. Today Proc.* **2020**, *20*, 50−53.

(10) Das, T.; Seo, D.; Seo, J. E.; Chang, J. Tunable Current Transport in PdSe2 via Layer-by-Layer Thickness Modulation by Mild Plasma. *Adv. Electron. Mater.* **2020**, *6* (5), 2000008.

(11) Liang, Q.; Zhang, Q.; Gou, J.; Song, T.; Arramel; Chen, H.; Yang, M.; Lim, S. X.; Wang, Q.; Zhu, R.; et al. Performance Improvement by Ozone Treatment of 2D PdSe2. *ACS Nano* **2020**, *14* (5), 5668−5677.

(12) Luo, W.; Oyedele, A. D.; Gu, Y.; Li, T.; Wang, X.; Haglund, A. V.; Mandrus, D.; Puretzky, A. A.; Xiao, K.; Liang, L.; et al. Anisotropic Phonon Response of Few-Layer PdSe2 under Uniaxial Strain. *Adv. Funct. Mater.* **2020**, *30* (35), 2003215.

(13) Puretzky, A. A.; Oyedele, A. D.; Xiao, K.; Haglund, A. V.; Sumpter, B. G.; Mandrus, D.; Geohegan, D. B.; Liang, L. Anomalous Interlayer Vibrations in Strongly Coupled Layered PdSe2. *2D Mater.* **2018**, *5* (3), 035016.

(14) Wu, J.; Mao, N.; Xie, L.; Xu, H.; Zhang, J. Identifying the Crystalline Orientation of Black Phosphorus Using Angle-Resolved

Polarized Raman Spectroscopy. *Angew. Chem., Int. Ed.* **2015**, *54* (8), 2366−2369.
(15) Ribeiro, H. B.; Pimenta, M. A.; De Matos, C. J.; Moreira, R. L.; Rodin, A. S.; Zapata, J. D.; De Souza, E. A.; Castro Neto, A. H. Unusual Angular Dependence of the Raman Response in Black Phosphorus. *ACS Nano* **2015**, *9* (4), 4270−4276.
(16) Ling, X.; Huang, S.; Hasdeo, E. H.; Liang, L.; Parkin, W. M.; Tatsumi, Y.; Nugraha, A. R. T.; Puretzky, A. A.; Das, P. M.; Sumpter, B. G.; Geohegan, D. B.; Kong, J.; Saito, R.; Drndic, M.; Meunier, V.; Dresselhaus, M. S. Anisotropic Electron-Photon and Electron-Phonon Interactions in Black Phosphorus. *Nano Lett.* **2016**, *16* (4), 2260−2267.
(17) Zhou, Y.; Maity, N.; Rai, A.; Juneja, R.; Meng, X.; Roy, A.; Zhang, Y.; Xu, X.; Lin, J.-F.; Banerjee, S. K.; et al. Stacking-Order-Driven Optical Properties and Carrier Dynamics in ReS2. *Adv. Mater.* **2020**, *32* (22), 1908311.
(18) Zhou, Y.; Maity, N.; Lin, J.-F.; Singh, A. K.; Wang, Y. Nonlinear Optical Absorption of ReS2 Driven by Stacking Order. *ACS Photonics* **2021**, *8* (2), 405−411.
(19) Upadhyay, P.; Maity, N.; Kumar, R.; Barman, P. K.; Singh, A. K.; Nayak, P. K. Layer Parity Dependent Raman-Active Modes and Crystal Symmetry in ReS 2. *Phys. Rev. B* **2022**, *105* (4), 045416.
(20) McCreary, A.; Simpson, J. R.; Wang, Y.; Rhodes, D.; Fujisawa, K.; Balicas, L.; Dubey, M.; Crespi, V. H.; Terrones, M.; Hight Walker, A. R. Intricate Resonant Raman Response in Anisotropic ReS2. *Nano Lett.* **2017**, *17* (10), 5897−5907.
(21) Gomes, L. C.; Trevisanutto, P. E.; Carvalho, A.; Rodin, A. S.; Castro Neto, A. Strongly Bound Mott-Wannier Excitons in GeS and GeSe Monolayers. *Phys. Rev. B* **2016**, *94* (15), 155428.
(22) Zhao, J.; Zeng, H.; Yao, G. Computational Design of a Polymorph for 2D III−V Orthorhombic Monolayers by First Principles Calculations: Excellent Anisotropic, Electronic and Optical Properties. *Phys. Chem. Chem. Phys.* **2021**, *23* (6), 3771−3778.
(23) Maity, N.; Srivastava, P.; Mishra, H.; Shinde, R.; Singh, A. K. Anisotropic Interlayer Exciton in Gese/Sns van Der Waals Heterostructure. *J. Phys. Chem. Lett.* **2021**, *12* (7), 1765−1771.
(24) Mao, N.; Wang, X.; Lin, Y.; Sumpter, B. G.; Ji, Q.; Palacios, T.; Huang, S.; Meunier, V.; Dresselhaus, M. S.; Tisdale, W. A.; et al. Direct Observation of Symmetry-Dependent Electron−Phonon Coupling in Black Phosphorus. *J. Am. Chem. Soc.* **2019**, *141* (48), 18994−19001.
(25) Kim, J.; Lee, J.-U.; Lee, J.; Park, H. J.; Lee, Z.; Lee, C.; Cheong, H. Anomalous Polarization Dependence of Raman Scattering and Crystallographic Orientation of Black Phosphorus. *Nanoscale* **2015**, *7* (44), 18708−18715.
(26) Luo, W. *Controllable and Scalable Thermal Sublimation Thinning of Black Phosphorus*. MASc Thesis, University of British Columbia, 2017.
(27) Zhao, Y.; Luo, X.; Li, H.; Zhang, J.; Araujo, P. T.; Gan, C. K.; Wu, J.; Zhang, H.; Quek, S. Y.; Dresselhaus, M. S.; et al. Interlayer Breathing and Shear Modes in Few-Trilayer MoS2 and WSe2. *Nano Lett.* **2013**, *13* (3), 1007−1015.
(28) Liang, L.; Zhang, J.; Sumpter, B. G.; Tan, Q.-H.; Tan, P.-H.; Meunier, V. Low-Frequency Shear and Layer-Breathing Modes in Raman Scattering of Two-Dimensional Materials. *ACS Nano* **2017**, *11* (12), 11777−11802.
(29) Wolverson, D.; Crampin, S.; Kazemi, A. S.; Ilie, A.; Bending, S. J. Raman Spectra of Monolayer, Few-Layer, and Bulk ReSe2: An Anisotropic Layered Semiconductor. *ACS Nano* **2014**, *8* (11), 11154−11164.
(30) Yu, J.; Kuang, X.; Gao, Y.; Wang, Y.; Chen, K.; Ding, Z.; Liu, J.; Cong, C.; He, J.; Liu, Z.; et al. Direct Observation of the Linear Dichroism Transition in Two-Dimensional Palladium Diselenide. *Nano Lett.* **2020**, *20* (2), 1172−1182.
(31) Kresse, G. G.; Furthmüller, J. Efficient iterative schemes for ab initio total-energy calculations using a plane-wave basis set. *Phys. Rev. B* **1996**, *54*, 11169.
(32) Kresse, G.; Furthmüller, J. Efficiency of Ab-Initio Total Energy Calculations for Metals and Semiconductors Using a Plane-Wave Basis Set. *Comput. Mater. Sci.* **1996**, *6* (1), 15−50.
(33) Perdew, J. P.; Ruzsinszky, A.; Csonka, G. I.; Vydrov, O. A.; Scuseria, G. E.; Constantin, L. A.; Zhou, X.; Burke, K. Restoring the Density-Gradient Expansion for Exchange in Solids and Surfaces. *Phys. Rev. Lett.* **2008**, *100*, 136406.
(34) Perdew, J. P.; Burke, K.; Ernzerhof, M. Generalized Gradient Approximation Made Simple. *Phys. Rev. Lett.* **1996**, *77*, 3865.
(35) Jain, A.; Ong, S. P.; Hautier, G.; Chen, W.; Richards, W. D.; Dacek, S.; Cholia, S.; Gunter, D.; Skinner, D.; Ceder, G.; et al. Commentary: The Materials Project: A Materials Genome Approach to Accelerating Materials Innovation. *Apl Mater.* **2013**, *1* (1), 011002.

https://doi.org/10.1021/acsphyschemau.2c00007
ACS Phys. Chem Au 2022, 2, 482−489